NANO LETTERS

pubs.acs.org/NanoLett Letter

Ferroelectric Domain and Switching Dynamics in Curved In_2Se_3: First-Principles and Deep Learning Molecular Dynamics Simulations

Dongyu Bai, Yihan Nie,* Jing Shang, Junxian Liu, Minghao Liu, Yang Yang, Haifei Zhan, Liangzhi Kou,* and Yuantong Gu*

Cite This: https://doi.org/10.1021/acs.nanolett.3c03160 Read Online

ACCESS | Metrics & More | Article Recommendations | Supporting Information

ABSTRACT: Despite its prevalence in experiments, the influence of complex strain on material properties remains understudied due to the lack of effective simulation methods. Here, the effects of bending, rippling, and bubbling on the ferroelectric domains are investigated in an In_2Se_3 monolayer by density functional theory and deep learning molecular dynamics simulations. Since the ferroelectric switching barrier can be increased (decreased) by tensile (compressive) strain, automatic polarization reversal occurs in α-In_2Se_3 with a strain gradient when it is subjected to bending, rippling, or bubbling deformations to create localized ferroelectric domains with varying sizes. The switching dynamics depends on the magnitude of curvature and temperature, following an Arrhenius-style relationship. This study not only provides a promising solution for cross-scale studies using deep learning but also reveals the potential to manipulate local polarization in ferroelectric materials through strain engineering.

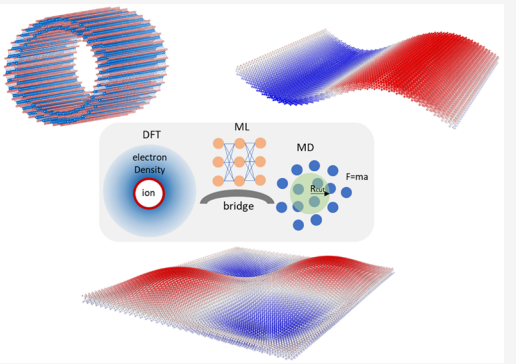

KEYWORDS: *2D ferroelectric, α-In_2Se_3, polarization switching, deep learning potential, strain engineering*

Over the past two decades, 2D materials have emerged as a new research hotspot, due to their unique physical and chemical properties, as well as promising applications in biosensors,[1,2] solar photovoltaics,[3] catalysis,[4−6] and electronic devices.[7−9] The atomic-thick structures distinguish them from their bulk counterparts in terms of distinct mechanical, thermal, and electrical properties. However, the weaker bending stiffness compared to their in-plane modulus[10] makes it easy to induce out-of-plane bending and crumpling, especially when being influenced by the substrate,[11−13] interface liquid,[14,15] and thermal strain.[16−18] In fact, the inevitable wrinkled structures have been commonly observed in graphene,[19] transition-metal dichalcogenides,[20] and black phosphorene. The corrugations have been shown to significantly affect the electronic, mechanical, electrical, and optical properties, thereby impacting the performance of associated devices.[21,22] For example, the crest of graphene's nanobubbles exhibits enhanced catalytic activity for the HER or ORR[23,24] than the area of flat graphene. The rippling deformation in MoS_2 has detrimental effects on electron mobility; removing them could result in optimal performance of the electronic device. Through proper strain engineering, the out-of-plane deformation can be used for optimizing performance or designing novel functional devices.[25,26]

2D ferroelectrics, such as In_2Se_3,[27−29] $MoTe_2$,[30] $CuInP_2S_6$,[31−33] and the SnTe family,[34−36] are a unique class of van der Waals materials that exhibit stable spontaneous and switchable polarization under external stimuli. Mechanical bending or rippling deformation can well couple with electric polarization due to the generated interlayer movement or ion migration,[27,37] leading to flexoelectric phenomena or ferroic domains that enable the measurement of strain gradient in mechanical structures electrically. Rippling/bending deformations therefore gain the ability to weaken, strengthen, or reverse polarization. For example, polarization vortex or polar skyrmions were realized at room temperature in ferroelectric bubbling domains induced by lattice mismatch strain in $(PbTiO_3)_n/(SrTiO_3)_n$ heterostructures.[38,39] Ripple-induced ferroic phase transition and domain switching have been observed in 2D ferroelectric GeSe layers, indicating their potential application in flexible electronics.[40] Despite their fundamental and practical importance, a deep understanding at the atomic level for the effect of wrinkles on polarization switching, especially in terms of out-of-plane ferroelectricity, remains scarce due to the lack of appropriate simulation methods and the requirements for extremely high resolution of experimental measurements.

Received: August 22, 2023
Revised: November 6, 2023
Accepted: November 9, 2023

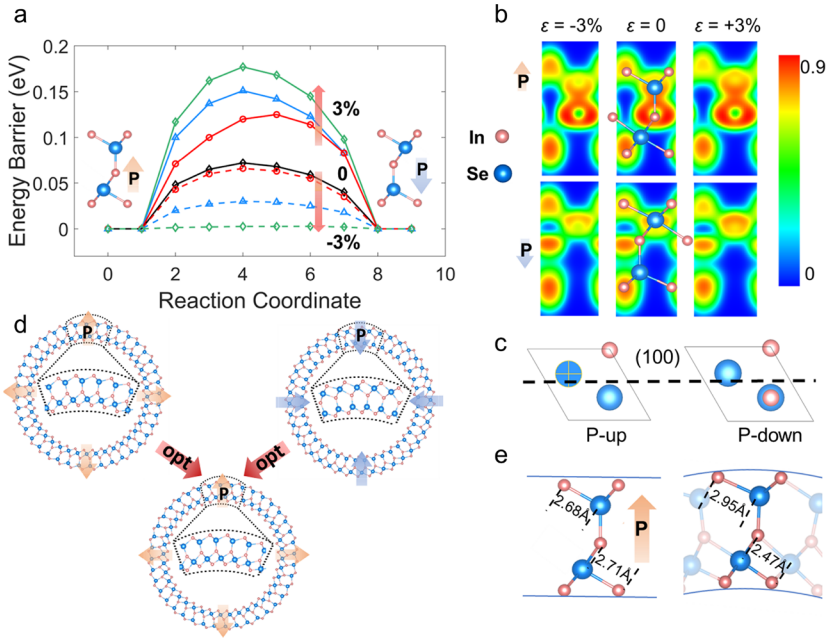

Figure 1. (a) Polarization switching barriers of monolayer α-In_2Se_3 under various in-plane strains. (b) Electron localization function (ELF) maps under in-plane strains. The upper and lower panels present the P↑ and P↓ In_2Se_3, respectively. (c) The atomic structures of cross sections corresponding to ELF maps of P↑ and P↓. (d) The initial and optimized structures of In_2Se_3 nanotubes from P↑ and P↓ states. (e) The variation of In−Se bond length before and after bending a nanotube with a radius of 22.60 Å.

Here, we revealed the impacts of bending, rippling, and bubbling deformations of α-In_2Se_3 on its ferroelectric polarization, based on density functional theory (DFT) and molecular dynamics (MD) simulations. The methodology details can be found in the Supporting Information and Figure S1. It is found that the ferroelectric switching barrier can be reduced/increased by uniaxial tensile/compressive strain, which enables automatic polarization reversal when tensile and compressive strains coexist. The switching dynamics in complex strain deformation is then studied with deep-learning potentials and large-scale MD simulations.[41−43] Ferroelectric domains can be created and switched by the rippling and bubbling deformations, and the switching time is dependent on the curvature and temperature. Our results provide a new approach for strain engineering of 2D ferroelectric materials as flexible electronic devices.

Switching Barrier Influenced by Strain. The spontaneous polarization in α-In_2Se_3 results from structural asymmetry along the out-of-plane direction, where the position of the central Se layer plays a critical role in determining the polarization orientation. A two-step in-plane shift of the central Se layer (ionic displacement) to overcome an energy barrier of 67 meV can cause the polarization to reverse (Figure S3b in the Supporting Information). The calculation is conducted within a lattice cell, and in a multilattice system influenced by the nucleation−growth mechanism, the energy barrier could experience further reduction compared to the unit cell DFT results.[27,44]

We first investigate the impact of uniaxial ±3% strain on the energy barrier, to lay a theoretical foundation for later analysis of complex strain, although it is probably challenging to achieve −3% compressive strain in reality. DFT calculations indicate that the energy barrier of ferroelectric switching can be significantly increased by the tensile strain. The value can be increased by ∼300% (Figure 1a) with 3% tensile strain but reduced to 0 eV with −3% compressive strain, implying that the polarization is easier/more difficult to switch under the compression/tensile strain. Different exchange correlation functions have the impacts on the values of ferroelectric switching but do not affect the conclusion (see Figure S2). The phenomena can be intuitively understood from structural deformation, where the thickness along the out-of-plane direction will expand under in-plane compression deformations to facilitate the motion of the Se layer. This can also be seen from the electron localization function (ELF) (Figure 1c). Taking the P↑ In_2Se_3 as an example, more localization of electrons is observed in the tensile case (+3%) than in the compressive model (−3%). Thus, the tensile state is less prone to switch polarization direction than the compressed state.

To verify the impacts of strain on the ionic displacement and associated phase transition, an In_2Se_3 nanotube with a radius of 22.6 Å is built to investigate the bending effect. 15 Å of vacuum layer is added in the radial direction, while periodicity is applied in the axial direction. Depending on the wrap direction, two models with initially opposite polarization states are constructed (Figure 1d). After the optimization, both are transformed into the same configuration, i.e., the polarization pointing toward outside as shown in Figure 1d. Due to the structural symmetry, the nanotube exhibits overall zero polarization and internal electric field due to the cancellation. The In−Se bond lengths are stretched to 2.95 Å at the outer layer (originally 2.68 Å) but compressed to 2.47 Å (originally 2.71 Å) at the inner layer (Figure 1e). The outside of the tube is subject to the tensile strain while the inner side is subject to the compressive strain. The central Se layer tends to move to the compression region since the polarization switching barrier is significantly lower under compressive strain as found in Figure 1a. Therefore, regardless of the initial polarization direction and structural models, the polarization direction in In_2Se_3 tubes always points outward after the structural optimization, and the central Se layer prefers to migrate to the compression side under bending conditions when both

https://doi.org/10.1021/acs.nanolett.3c03160
Nano Lett. XXXX, XXX, XXX−XXX

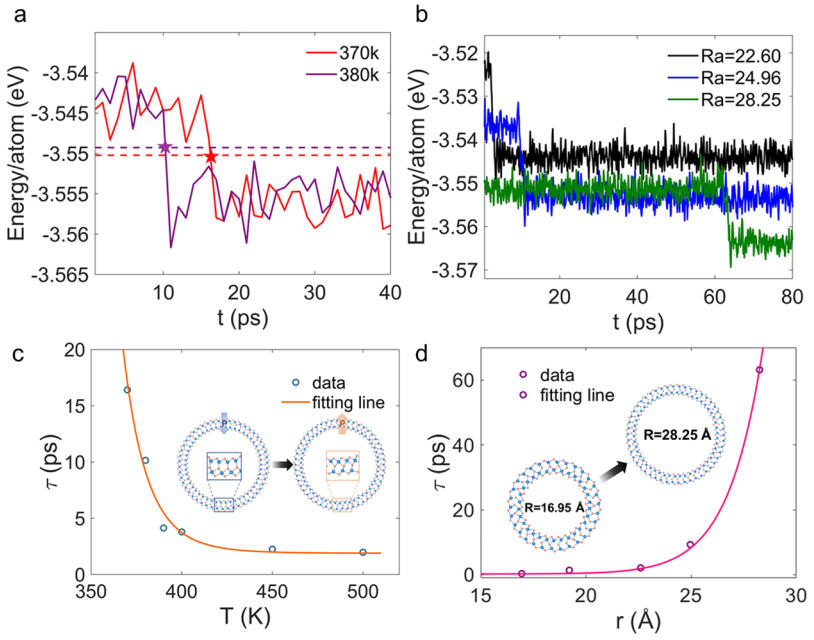

Figure 2. DLMD results for In_2Se_3 nanotubes. (a) Energy variation for a tube with a radius of 28.25 Å at different temperatures, represented by the solid lines. The dashed line is the average value between the two polarization states. (b) Energy variations with time for nanotubes with radii from 22.60 to 28.25 Å at 300 K. (c) Switching time τ as a function of temperature and its fitting curve for nanotubes with a radius of 28.25 Å. The insets are the nanotube configurations before and after the polarization switching. (d) Switching time τ as a function of different radii and its fitting curve for nanotube at 300 K. The illustration is the configurations of tubes with radii of 16.95 and 28.25 Å after the polarization switching.

tensile and compressive strains coexist. Besides the ionic-displacement-induced polarization reversal, it is worth noticing that the flexoelectric effect from a bending-induced strain gradient is also a potential trigger for polarization switching as found in MoS_2.[45−47] We therefore calculate the polarization contribution in bent In_2Se_3 induced by the flexoelectric effect to elucidate the primary mechanism behind polarization reversal. Calculations demonstrate that at a curvature radius of 22.60 Å, the flexoelectric-effect-induced polarization accounts for 24.29% of the overall polarization value. The proportion significantly diminishes as a function of the reciprocal of the radius, reaching only 10.98% at a curvature radius of 50 Å. This indicates that the dominant mechanism governing polarization switching is ionic displacement (the shift in the central Se layer), but not the flexoelectric effect (refer to Figures S4 and S5). Given that the curvature radius is much larger in rippling and bubbling deformations (see below), we will disregard the flexoelectric-induced polarization and reversal in subsequent analysis.

Validation of Deep Learning Potential. To study complex strain and nonuniform deformation, we developed the force fields of In_2Se_3 with the DeepMD-kit.[41] The training set is based on open-source data from the recent work by Wu et al.,[48] which was generated by DP-GEN and contained 22600 monolayer structures such as α, β, β', β_1', and β_2' phases and 2163 bulk structures. Besides DeepMD and DP-GEN, the alternative choice can be active machine learning potential packages that can accelerate the database setup process.[49,50] Details of the potential training including the descriptor, training neuron layers, and accuracy can be found from the section 1 in the Supporting Information. Our benchmark calculations indicate that the potential performs remarkably well in both energy and force predictions. Across nearly 8500 examples, the mean absolute error (MAE) is around 3.9 meV/atom (Figure S6). Significantly, the deep learning potential can accurately predict the energy barrier under various strain conditions and phase transitions, demonstrating remarkable consistency with previous DFT results (Figures S2, S6, and S7). All MD simulations below are based on this deep learning force field and are implemented in LAMMPS software.

Switching Dynamics under Pure Bending. Although a DFT simulation can accurately predict the polarization reversal behaviors, it does not consider thermal disturbance from the environments. Based on the trained force field, we are able to study the switching dynamics and complex systems at various temperatures. We first study the In_2Se_3 nanotube with a radius of 28.25 Å from the MD simulation. Consistent with DFT simulations, the polarization which initially points inside is reversed after the structural relaxation, with a sudden energy drop, as seen in Figure 2a and Figure S8. The switching time τ (defined as the time for the total energy to decrease to the average energy of the two states) is 17 ps at 370 K (Figure 2a) but decreases to 10 ps when the temperature was increased to 380 K, indicating that the switching process is accelerated by the increased thermal disturbance. The underlying mechanism can be attributed to the increased kinetic energy of the atoms, which enhances the likelihood of overcoming the energy barrier and accelerates ferroelectric switching. The switching time τ exhibits an exponential relationship with temperature (see Figure 2c). Since the process is akin to chemical reactions, where the energy barrier of ferroelectric switching corresponds to the activation energy, the switching time should be the reciprocal of the reaction rate. It could be thus effectively modeled using an Arrhenius-style equation

$$\tau = Ae^{E_b/k_bT} + t_m \quad (1)$$

where A is the amplitude fitted as 9.57×10^{-12} ps, E_b is the energy barrier fitted as 0.895 eV and the constant t_m equals 1.90 ps, k_b is the Boltzmann constant, and T is the temperature. The constant t_m indicates that for a certain

https://doi.org/10.1021/acs.nanolett.3c03160
Nano Lett. XXXX, XXX, XXX−XXX

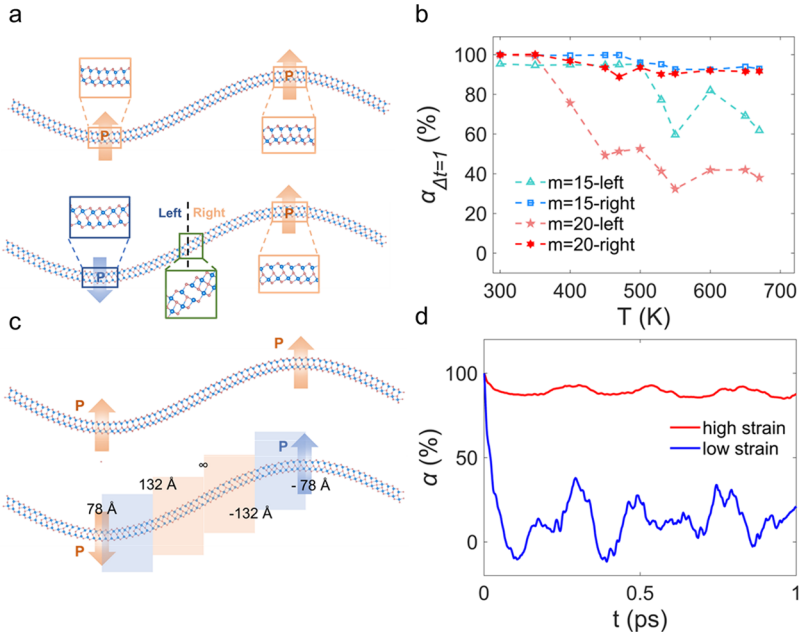

Figure 3. Ferroelectric domain and dynamics in rippling models. (a) The monolayer rippling configuration with m = 20 Å at 450 K. The top/bottom image represents the structure at 0/85 ps. (b) The polarization correlation of left and right regions at 1 ps as a function of temperature. (c) Division of the rippling model into high-strain and low-strain regions, with corresponding curvature radii indicated. (d) Temporal variation of polarization correlation in different strain regions.

curvature there is a minimal time to achieve the switching process.

Another factor affecting the switching dynamics is the bending curvature. The switching time τ for nanotubes with radii of 22.6, 24.96, and 28.25 Å are simulated under 300 K (Figure 2b and Figure S9) to study the size effect. The polarization reversal takes 3 ps for the smallest tube (R = 22.6 Å) but much longer for the other two (10 ps for R = 24.96 Å and 63 ps for R = 28.25 Å, respectively). After taking the curvature radius into the consideration, the Arrhenius-style equation (eq 1) can be revised and updated as

$$\tau = Be^{l_e\sqrt{r}/k_bT} + t_m \tag{2}$$

where E_b in the eq 1 can be replaced as $l_e\sqrt{r}$. The amplitude B equals 6.245×10^{-14} ps, l_e is the coefficient for energy barrier 0.168 eV/Å$^{1/2}$, r is the radius of the nanotube model, and t_m equals 0.25 ps, as a minimal time for switching process at 300 K. The fitting equation indicates a linear relationship between the energy barrier and the 1/2 power of the radius of curvature (see Figure 2d). Both equations give similar energy barrier prediction values, i.e., 0.89 eV, for the nanotube with radius of 28.25 Å.

Switching Dynamics with Rippling Deformation and the Lifetime of the Transient Polarization. Rippling deformation is commonly observed in 2D materials when compression forces are experienced at the boundary. Here, a monosinusoidal-shaped model with periodic boundary conditions in the in-plane direction is created to mimic rippling deformation. The thermal impacts of temperatures (ranging from 300 to 670 K) and size effects of rippling amplitudes (m = 15 and m = 20 Å) are studied. After structural relaxation, a prominent phase transition occurs in the left region, which is situated in the wave trough with a positive curvature. This phase transition is caused by the ionic displacement of the central Se layer, resulting in a polarization switching from [001] to [00−1], similar to the phenomenon observed in nanotubes (Figure 2). In contrast, the polarization in the right region, located at the wave crest with a negative strain curvature, remains unchanged throughout the process. Therefore, the local polarization and induced electric field due to the nonuniform distribution have opposite preference direction in the two regions, resulting in localized ferroelectric domains. They are separated by the boundary (dashed line in Figure 3a) characterized with a paraelectric β phase, as indicated by the enlarged local structure. These structural phase transitions and localized polarization reversals are also observed in other models with different rippling amplitudes (m = 15 Å) and temperatures (Figures S10 and S11).

As a dynamic process, the local polarization lifetime and the stability of ferroelectric domains are investigated by tracking the autocorrelation functions of local momentum. The method has been employed to experimentally measure the lifetime of polarization from voltage-modulated scanning force microscopy which can analyze transient local polarization and subsequently process the obtained data mathematically.[51] The autocorrelation function is defined as

$$\alpha(t) = \frac{\left\langle \int \vec{D}_I(t_0)\vec{D}(t_0 + t)\, dt_0 \right\rangle}{\alpha_i(0)} \tag{3}$$

to describe the proportion of polarization that can maintain its original direction over the time interval of t. $\vec{D}_I(t_0)$ is the value of the dipole moment of chunk i at t_0. t is the time interval. The autocorrelation function at the starting point $\alpha_i(0)$ is normalized to 1, namely, all the polarizations at the beginning point to the same direction. After the time interval (1 ps in Figure 3b), we calculate the ratio which preserves the original direction (namely, the autocorrelation); a low/high value indicates a short/long lifetime of the ferroelectric domain. Figure 3a illustrates the polarization switching behavior in the ripple model before and after structural relaxation; the different

https://doi.org/10.1021/acs.nanolett.3c03160
Nano Lett. XXXX, XXX, XXX−XXX

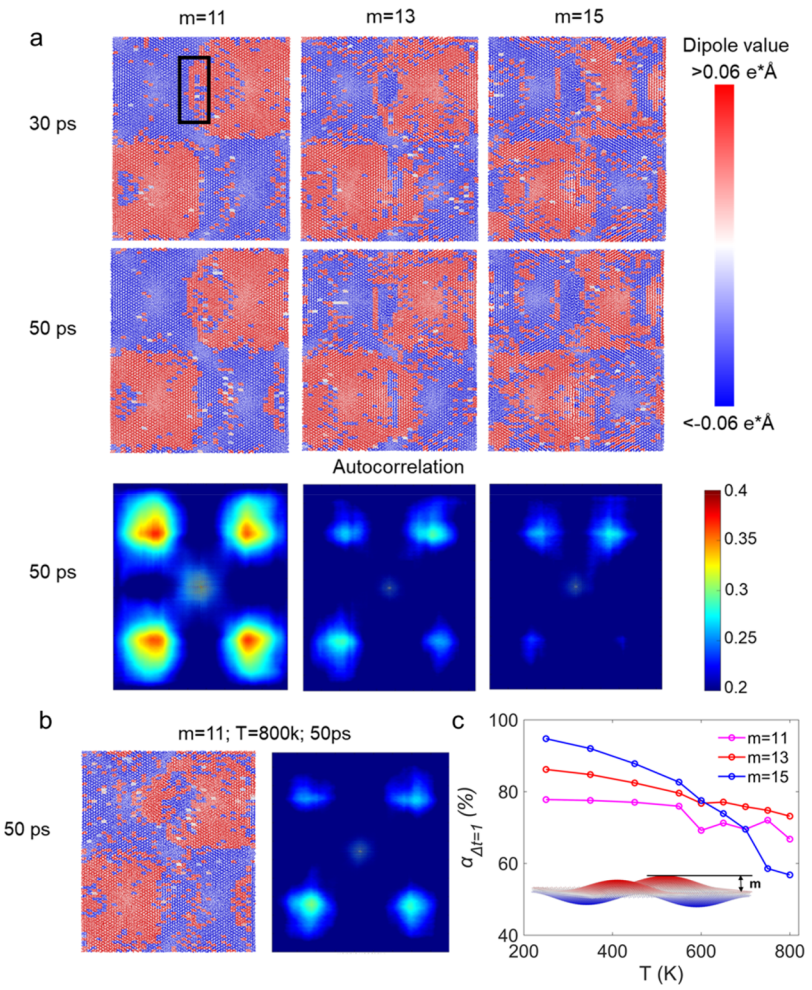

Figure 4. (a) The polarization distribution during relaxation and autocorrelation maps at m = 11, 13, and 15 at 450 K in the bubbling model. The boundary of the domain is the intersection between the red and blue regions, using the image contained within the rectangular box as an illustrative example. (b) The polarization distribution at 50 ps and autocorrelation map at m = 11 at 800 K in the bubbling model. (c) Structural stability $\alpha_{\Delta t}$ = 1 of different m with temperature and its trend line in the bubbling model.

autocorrelation functions are observed at left and right regions. The autocorrelation at the left region remains almost unchanged until the temperature reaches 500 K when the ripple attitude m = 15 Å but significantly decreases to around 60% at 550 K. In contrast, it maintains as a constant value in the right region even when the temperature is increased to 700 K. The results imply that polarization reversal occurs only at the ripple wave trough after 1 ps when reaching a critical temperature, but not at the wave crest (Figure 3b). This finding holds true at a larger rippling amplitude like m = 20 Å. However, both the critical temperature (350 K) and autocorrelation (only 30% at 550 K) in the left region are much lower than the corresponding values when m = 15 Å. Consequently, the ripple amplitude can thus act as an effective parameter to facilitate the polarization switching and control the lifetime of the ferroelectric domain.

Since ripple deformation will lead to a complex and nonuniform strain distribution, we also analyze and compare the transient polarization behavior in regions with different curvatures. Following relaxation, the ripple model with m = 20 Å is divided into several distinct areas as shown in Figure 3c. The radius of curvature falls between 78 and 132 Å in the high-strain region but exceeds 132 Å in the low-strain region. The calculated autocorrelation at 450 K clearly illustrates that the polarization lifetime in the high-strain region is notably longer than that in the low-strain region, with the latter being like transient polarization behavior (Figure 3d).

Switching Dynamics with Bubbling Deformation and the Ferroelectric Domain. For bubbling deformation, it is mimicked by the dual sinusoidal model with boundary conditions similar to those of the ripple model. More details about the models and calculation methods can be found in sections 2 and 3 in the Supporting Information.

As shown in Figure 4a, the polarization distribution at 450 K is presented for the bubble amplitudes of 11, 13, and 15 Å. After 30 ps structural relaxation for the model with m = 11 Å, the adjacent twin domains are found with clear opposite polarizations, as indicated by red and blue colors. Although the polarizations at the boundary regions are affected by thermal fluctuations, the overall distribution can be well maintained up to 50 ps. When the bubble amplitude is increased to 13 or 15 Å, the continuity of the ferroelectric domain is noticeably diminished. The crest (trough) still exhibits positive (negative) polarization, although the domain size obviously shrinks.

The influence of bubble amplitude on the continuity of the polarization domain size can be intuitively confirmed by image autocorrelation analysis, as shown in the bottom panels of Figure 4a. Brighter regions indicate a higher degree of self-

https://doi.org/10.1021/acs.nanolett.3c03160
Nano Lett. XXXX, XXX, XXX−XXX

similarity and stronger correlation, corresponding to the areas with the larger size of the polarization domain or the continuity of the polarization domain. It is found that an increased m results in a decrease in brightness at the crest of the autocorrelation image, indicating the disruption of the continuity of the polarized domains or a reduction in the size of the positively polarized domains at the crest (Figure S12).

The examination of relaxation studies at various temperature reveals its substantial influence on ferroelectric domains, wherein higher temperatures notably diminish the size of the local polarization domain (see Figure 4b and Figure S13). For instance, at 800 K, the local polarization distribution is disrupted after 50 ps structural relaxation, leading to a homogeneous mixture and uniform distribution of different domains because the ferroelectricity of In_2Se_3 disappeared over the Curie temperature.[52]

The influence of the temperature and bubbling amplitude on the ferroelectric domain can be more clearly seen when we specifically exclude the impact of tensile effects. Here, the autocorrelation function is utilized to analyze the polarization lifetime within the high-strain region of the bubbling model (Figures S14 and S15 and Figure 4c). Under the same strain conditions, $\alpha_{\Delta t} = 1$ exhibits lower values at higher temperatures, indicating that the local polarization stability decreases when the temperature increases. Concurrently, the bubbling amplitude demonstrates a positive impact on stability under consistent temperature conditions. An increased strain gradient (corresponding to an increased bubbling amplitude value) leads to a higher $\alpha_{\Delta t} = 1$, namely, the longer lifetime in the polarization domain. For example, the value is 77% when m = 11 Å at 250 K but increases to 86% and 94% as the amplitude m = 13 and 15 Å, respectively. These results confirm that in the large bubbling model of In_2Se_3, the previous relation between polarization stability and curvature still remains.

In summary, we report the polarization switching and its dynamics in curved In_2Se_3 through joint DFT and DLMD simulations. Ferroelectric In_2Se_3 will undergo an automatic polarization reversal under pure bending; the switching time is dependent on the environmental temperature and bending curvature. Research conducted using complex rippling and bubbling models reveals that lower temperatures and elevated bending strain foster larger domain sizes and longer lifetimes. Our research offers a promising approach for investigating strain effects on polarization dynamics of ferroelectric materials by conducting cross-scale simulations, and it provides valuable insights for the controlling polarization characteristics of ferroelectric materials by strain engineering in device fabrication.

■ ASSOCIATED CONTENT

Supporting Information

The Supporting Information is available free of charge at https://pubs.acs.org/doi/10.1021/acs.nanolett.3c03160.

Details for DL potential training, methods of model construction, computational details of DFT and MD simulations, validation results for DL potential, and additional results for nanotube, rippling, and bubbling models (PDF)

■ AUTHOR INFORMATION

Corresponding Authors

Yihan Nie − *School of Mechanical, Medical and Process Engineering, Queensland University of Technology, Brisbane, Queensland 4001, Australia; College of Civil Engineering and Architecture, Zhejiang University, Hangzhou 310058, People's Republic of China*; Email: Yihan.nie@zju.edu.cn

Yuantong Gu − *School of Mechanical, Medical and Process Engineering, Queensland University of Technology, Brisbane, Queensland 4001, Australia*; Email: yuantong.gu@qut.edu.au

Liangzhi Kou − *School of Mechanical, Medical and Process Engineering, Queensland University of Technology, Brisbane, Queensland 4001, Australia*; orcid.org/0000-0002-3978-117X; Email: Liangzhi.kou@qut.edu.au

Authors

Dongyu Bai − *School of Mechanical, Medical and Process Engineering, Queensland University of Technology, Brisbane, Queensland 4001, Australia*; orcid.org/0000-0001-8695-454X

Jing Shang − *School of Materials Science and Engineering, Shaanxi University of Science and Technology, Xi'an 710021, People's Republic of China*

Junxian Liu − *School of Mechanical, Medical and Process Engineering, Queensland University of Technology, Brisbane, Queensland 4001, Australia*; orcid.org/0000-0002-5873-0095

Minghao Liu − *School of Mechanical, Medical and Process Engineering, Queensland University of Technology, Brisbane, Queensland 4001, Australia*

Yang Yang − *State Key Laboratory for Mechanical Behavior of Materials, Xi'an Jiaotong University, Xi'an 710049, People's Republic of China*

Haifei Zhan − *College of Civil Engineering and Architecture, Zhejiang University, Hangzhou 310058, People's Republic of China*

Complete contact information is available at: https://pubs.acs.org/10.1021/acs.nanolett.3c03160

Author Contributions

L.K. conceived the idea and supervised the research with Y.G. D.B. and Y.N. jointly designed the simulation process and models. D.B. trained the DLMD potential and conducted the MD simulations, assisted by Y.Y. and H.Z. J.S., J.L., and M.L. executed the DFT simulations. D.B. analyzed the data and composed the manuscript. All authors have given approval to the final version of the manuscript.

Notes

The authors declare no competing financial interest.

■ ACKNOWLEDGMENTS

This work was supported by the Australian Research Council (Grant IC190100020 and DP200102546 & DP230101904), the National Natural Science Foundation of China (Grant 12202254), and the High-performance Computing (HPC) resources provided by the Queensland University of Technology (QUT). This research was undertaken with assistance of resources and services from the National Computational Infrastructure (NCI), which is supported by the Australian Government.

https://doi.org/10.1021/acs.nanolett.3c03160
Nano Lett. XXXX, XXX, XXX−XXX

ABBREVIATIONS

HER, hydrogen evolution reaction; OER, oxygen evolution reaction; DFT, density functional theory; DLMD, deep learning molecular dynamics

REFERENCES

(1) Lei, Z. L.; Guo, B. 2D Material-Based Optical Biosensor: Status and Prospect. *Adv. Sci.* **2022**, *9* (4), 2102924.

(2) Chen, F.; Tang, Q.; Ma, T.; Zhu, B.; Wang, L.; He, C.; Luo, X.; Cao, S.; Ma, L.; Cheng, C. Structures, properties, and challenges of emerging 2D materials in bioelectronics and biosensors. *InfoMat* **2022**, *4* (5), No. e12299.

(3) Das, S.; Pandey, D.; Thomas, J.; Roy, T. The role of graphene and other 2D materials in solar photovoltaics. *Adv. Mater.* **2019**, *31* (1), 1802722.

(4) Shifa, T. A.; Wang, F.; Liu, Y.; He, J. Heterostructures based on 2D materials: A versatile platform for efficient catalysis. *Adv. Mater.* **2019**, *31* (45), 1804828.

(5) Tang, L.; Meng, X.; Deng, D.; Bao, X. Confinement catalysis with 2D materials for energy conversion. *Adv. Mater.* **2019**, *31* (50), 1901996.

(6) Zhang, X.; Chen, A.; Chen, L.; Zhou, Z. 2D materials bridging experiments and computations for electro/photocatalysis. *Adv. Energy Mater.* **2022**, *12* (4), 2003841.

(7) Zhang, L.; Zhou, J.; Li, H.; Shen, L.; Feng, Y. P. Recent progress and challenges in magnetic tunnel junctions with 2D materials for spintronic applications. *Appl. Phys. Rev.* **2021**, *8* (2), 021308.

(8) Liu, Y.; Zeng, C.; Zhong, J.; Ding, J.; Wang, Z. M.; Liu, Z. Spintronics in two-dimensional materials. *Nanomicro Lett.* **2020**, *12*, 1−26.

(9) Qi, L.; Ruan, S.; Zeng, Y.-J. Review on Recent Developments in 2D Ferroelectrics: Theories and Applications. *Adv. Mater.* **2021**, *33* (13), 2005098.

(10) Zhang, Z.; Yang, Y.; Penev, E. S.; Yakobson, B. I. Elasticity, flexibility, and ideal strength of borophenes. *Adv. Funct. Mater.* **2017**, *27* (9), 1605059.

(11) Kim, J.; Park, H.; Hannon, J. B.; Bedell, S. W.; Fogel, K.; Sadana, D. K.; Dimitrakopoulos, C. Layer-resolved graphene transfer via engineered strain layers. *Science* **2013**, *342* (6160), 833−836.

(12) Jiang, Y.; Mao, J.; Duan, J.; Lai, X.; Watanabe, K.; Taniguchi, T.; Andrei, E. Y. Visualizing strain-induced pseudomagnetic fields in graphene through an hBN magnifying glass. *Nano Lett.* **2017**, *17* (5), 2839−2843.

(13) Reserbat-Plantey, A.; Kalita, D.; Han, Z.; Ferlazzo, L.; Autier-Laurent, S.; Komatsu, K.; Li, C.; Weil, R.; Ralko, A.; Marty, L.; et al. Strain superlattices and macroscale suspension of graphene induced by corrugated substrates. *Nano Lett.* **2014**, *14* (9), 5044−5051.

(14) Ghorbanfekr-Kalashami, H.; Vasu, K.; Nair, R. R.; Peeters, F. M.; Neek-Amal, M. Dependence of the shape of graphene nanobubbles on trapped substance. *Nat. Commun.* **2017**, *8* (1), 15844.

(15) Chen, Z.; Leng, K.; Zhao, X.; Malkhandi, S.; Tang, W.; Tian, B.; Dong, L.; Zheng, L.; Lin, M.; Yeo, B. S.; et al. Interface confined hydrogen evolution reaction in zero valent metal nanoparticles-intercalated molybdenum disulfide. *Nat. Commun.* **2017**, *8* (1), 14548.

(16) Jiang, H.; Khang, D.-Y.; Song, J.; Sun, Y.; Huang, Y.; Rogers, J. A. Finite deformation mechanics in buckled thin films on compliant supports. *Proc. Natl. Acad. Sci. U.S.A.* **2007**, *104* (40), 15607−15612.

(17) Chen, P. Y.; Sodhi, J.; Qiu, Y.; Valentin, T. M.; Steinberg, R. S.; Wang, Z.; Hurt, R. H.; Wong, I. Y. Multiscale graphene topographies programmed by sequential mechanical deformation. *Adv. Mater.* **2016**, *28* (18), 3564−3571.

(18) Zhang, Q.; Yin, J. Spontaneous buckling-driven periodic delamination of thin films on soft substrates under large compression. *Journal of the Mechanics and Physics of Solids* **2018**, *118*, 40−57.

(19) Huang, Y.; Wang, X.; Zhang, X.; Chen, X.; Li, B.; Wang, B.; Huang, M.; Zhu, C.; Zhang, X.; Bacsa, W. S.; et al. Raman spectral band oscillations in large graphene bubbles. *Phys. Rev. Lett.* **2018**, *120* (18), 186104.

(20) Brivio, J.; Alexander, D. T.; Kis, A. Ripples and layers in ultrathin MoS2 membranes. *Nano Lett.* **2011**, *11* (12), 5148−5153.

(21) Kretinin, A.; Cao, Y.; Tu, J.; Yu, G.; Jalil, R.; Novoselov, K.; Haigh, S.; Gholinia, A.; Mishchenko, A.; Lozada, M.; et al. Electronic properties of graphene encapsulated with different two-dimensional atomic crystals. *Nano Lett.* **2014**, *14* (6), 3270−3276.

(22) Pizzocchero, F.; Gammelgaard, L.; Jessen, B. S.; Caridad, J. M.; Wang, L.; Hone, J.; Bøggild, P.; Booth, T. J. The hot pick-up technique for batch assembly of van der Waals heterostructures. *Nat. Commun.* **2016**, *7* (1), 11894.

(23) Deng, S.; Berry, V. Wrinkled, rippled and crumpled graphene: an overview of formation mechanism, electronic properties, and applications. *Mater. Today* **2016**, *19* (4), 197−212.

(24) Sun, P.; Xiong, W.; Bera, A.; Timokhin, I.; Wu, Z.; Mishchenko, A.; Sellers, M.; Liu, B.; Cheng, H.; Janzén, E.; et al. Unexpected catalytic activity of nanorippled graphene. *Proc. Natl. Acad. Sci. U.S.A.* **2023**, *120* (12), No. e2300481120.

(25) Klimov, N. N.; Jung, S.; Zhu, S.; Li, T.; Wright, C. A.; Solares, S. D.; Newell, D. B.; Zhitenev, N. B.; Stroscio, J. A. Electromechanical properties of graphene drumheads. *Science* **2012**, *336* (6088), 1557−1561.

(26) Branny, A.; Kumar, S.; Proux, R.; Gerardot, B. D. Deterministic strain-induced arrays of quantum emitters in a two-dimensional semiconductor. *Nat. Commun.* **2017**, *8* (1), 15053.

(27) Ding, W.; Zhu, J.; Wang, Z.; Gao, Y.; Xiao, D.; Gu, Y.; Zhang, Z.; Zhu, W. Prediction of intrinsic two-dimensional ferroelectrics in In2Se3 and other III2-VI3 van der Waals materials. *Nat. Commun.* **2017**, *8*, 14956.

(28) Zhou, Y.; Wu, D.; Zhu, Y.; Cho, Y.; He, Q.; Yang, X.; Herrera, K.; Chu, Z.; Han, Y.; Downer, M. C.; et al. Out-of-plane piezoelectricity and ferroelectricity in layered α-In2Se3 nanoflakes. *Nano Lett.* **2017**, *17* (9), 5508−5513.

(29) Cui, C.; Hu, W.-J.; Yan, X.; Addiego, C.; Gao, W.; Wang, Y.; Wang, Z.; Li, L.; Cheng, Y.; Li, P.; et al. Intercorrelated in-plane and out-of-plane ferroelectricity in ultrathin two-dimensional layered semiconductor In2Se3. *Nano Lett.* **2018**, *18* (2), 1253−1258.

(30) Yuan, S.; Luo, X.; Chan, H. L.; Xiao, C.; Dai, Y.; Xie, M.; Hao, J. Room-temperature ferroelectricity in MoTe2 down to the atomic monolayer limit. *Nat. Commun.* **2019**, *10* (1), 1−6.

(31) Deng, J.; Liu, Y.; Li, M.; Xu, S.; Lun, Y.; Lv, P.; Xia, T.; Gao, P.; Wang, X.; Hong, J. Thickness-Dependent In-Plane Polarization and Structural Phase Transition in van der Waals Ferroelectric CuInP2S6. *Small* **2020**, *16* (1), 1904529.

(32) Liu, F.; You, L.; Seyler, K. L.; Li, X.; Yu, P.; Lin, J.; Wang, X.; Zhou, J.; Wang, H.; He, H. Room-temperature ferroelectricity in CuInP2S6 ultrathin flakes. *Nat. Commun.* **2016**, *7* (1), 1−6.

(33) Xu, D.-D.; Ma, R.-R.; Fu, A.-P.; Guan, Z.; Zhong, N.; Peng, H.; Xiang, P.-H.; Duan, C.-G. Ion adsorption-induced reversible polarization switching of a van der Waals layered ferroelectric. *Nat. Commun.* **2021**, *12* (1), 655.

(34) Chang, K.; Liu, J.; Lin, H.; Wang, N.; Zhao, K.; Zhang, A.; Jin, F.; Zhong, Y.; Hu, X.; Duan, W.; et al. Discovery of robust in-plane ferroelectricity in atomic-thick SnTe. *Science* **2016**, *353* (6296), 274−278.

(35) Bao, Y.; Song, P.; Liu, Y.; Chen, Z.; Zhu, M.; Abdelwahab, I.; Su, J.; Fu, W.; Chi, X.; Yu, W.; et al. Gate-tunable in-plane ferroelectricity in few-layer SnS. *Nano Lett.* **2019**, *19* (8), 5109−5117.

(36) Higashitarumizu, N.; Kawamoto, H.; Lee, C.-J.; Lin, B.-H.; Chu, F.-H.; Yonemori, I.; Nishimura, T.; Wakabayashi, K.; Chang, W.-H.; Nagashio, K. Purely in-plane ferroelectricity in monolayer SnS at room temperature. *Nat. Commun.* **2020**, *11* (1), 1−9.

(37) Chen, C.; Liu, H.; Lai, Q.; Mao, X.; Fu, J.; Fu, Z.; Zeng, H. Large-Scale Domain Engineering in Two-Dimensional Ferroelectric CuInP2S6 via Giant Flexoelectric Effect. *Nano Lett.* **2022**, *22* (8), 3275−3282.

(38) Das, S.; Tang, Y.; Hong, Z.; Gonçalves, M.; McCarter, M.; Klewe, C.; Nguyen, K.; Gómez-Ortiz, F.; Shafer, P.; Arenholz, E.;

https://doi.org/10.1021/acs.nanolett.3c03160
Nano Lett. XXXX, XXX, XXX−XXX

et al. Observation of room-temperature polar skyrmions. *Nature* **2019**, *568* (7752), 368−372.
(39) Zhang, Q.; Xie, L.; Liu, G.; Prokhorenko, S.; Nahas, Y.; Pan, X.; Bellaiche, L.; Gruverman, A.; Valanoor, N. Nanoscale bubble domains and topological transitions in ultrathin ferroelectric films. *Adv. Mater.* **2017**, *29* (46), 1702375.
(40) Yang, Y.; Zong, H.; Sun, J.; Ding, X. Rippling Ferroic Phase Transition and Domain Switching In 2D Materials. *Adv. Mater.* **2021**, *33* (49), No. e2103469.
(41) Wang, H.; Zhang, L.; Han, J.; E, W. DeePMD-kit: A deep learning package for many-body potential energy representation and molecular dynamics. *Comput. Phys. Commun.* **2018**, *228*, 178−184.
(42) Larsen, A. H.; Mortensen, J. J.; Blomqvist, J.; Castelli, I. E.; Christensen, R.; Dułak, M.; Friis, J.; Groves, M. N.; Hammer, B.; Hargus, C.; et al. The atomic simulation environment—a Python library for working with atoms. *J. Phys.: Condens. Matter* **2017**, *29* (27), 273002.
(43) Kolb, B.; Lentz, L. C.; Kolpak, A. M. Discovering charge density functionals and structure-property relationships with PROPhet: A general framework for coupling machine learning and first-principles methods. *Sci. Rep.* **2017**, *7* (1), 1−9.
(44) Wang, H.; Qian, X. Two-dimensional multiferroics in monolayer group IV monochalcogenides. *2D Mater.* **2017**, *4* (1), 015042.
(45) Morozovska, A. N.; Eliseev, E. A.; Dovbeshko, G. I.; Glinchuk, M. D.; Kim, Y.; Kalinin, S. V. Flexoinduced ferroelectricity in low-dimensional transition metal dichalcogenides. *Phys. Rev. B* **2020**, *102* (7), 075417.
(46) Morozovska, A. N.; Eliseev, E. A.; Shevliakova, H. V.; Lopatina, Y. Y.; Dovbeshko, G. I.; Glinchuk, M. D.; Kim, Y.; Kalinin, S. V. Correlation between corrugation-induced flexoelectric polarization and conductivity of low-dimensional transition metal dichalcogenides. *Physical Review Applied* **2021**, *15* (4), 044051.
(47) Shevliakova, H. V.; Yesylevskyy, S. O.; Kupchak, I.; Dovbeshko, G. I.; Kim, Y.; Morozovska, A. N. Flexoelectric and piezoelectric coupling in a bended MoS2 monolayer. *Symmetry* **2021**, *13* (11), 2086.
(48) Wu, J.; Bai, L.; Huang, J.; Ma, L.; Liu, J.; Liu, S. Accurate force field of two-dimensional ferroelectrics from deep learning. *Phys. Rev. B* **2021**, *104* (17), 174107.
(49) Mortazavi, B.; Javvaji, B.; Shojaei, F.; Rabczuk, T.; Shapeev, A. V.; Zhuang, X. Exceptional piezoelectricity, high thermal conductivity and stiffness and promising photocatalysis in two-dimensional MoSi2N4 family confirmed by first-principles. *Nano Energy* **2021**, *82*, 105716.
(50) Mortazavi, B.; Silani, M.; Podryabinkin, E. V.; Rabczuk, T.; Zhuang, X.; Shapeev, A. V. First-principles multiscale modeling of mechanical properties in graphene/borophene heterostructures empowered by machine-learning interatomic potentials. *Adv. Mater.* **2021**, *33* (35), 2102807.
(51) Likodimos, V.; Labardi, M.; Allegrini, M. Kinetics of ferroelectric domains investigated by scanning force microscopy. *Phys. Rev. B* **2000**, *61* (21), 14440.
(52) Liu, J.; Pantelides, S. Pyroelectric response and temperature-induced α-β phase transitions in α-In2Se3 and other α-III2VI3 (III= Al, Ga, In; VI= S, Se) monolayers. *2D Mater.* **2019**, *6* (2), 025001.

https://doi.org/10.1021/acs.nanolett.3c03160
Nano Lett. XXXX, XXX, XXX−XXX